

Virtual melting as a new mechanism of stress relaxation under high strain rate loading

Valery I. Levitas^{a,1} and Ramon Ravelo^{b,c}

^aDepartments of Aerospace Engineering, Mechanical Engineering, and Material Science and Engineering, Iowa State University, Ames, IA 50011;

^bPhysics Department and Materials Research Institute, University of Texas, El Paso, TX 79968; and ^cComputational Physics Division, Los Alamos National Laboratory, Los Alamos, NM 87545

Edited by* William A. Goddard III, California Institute of Technology, Pasadena, CA, and approved June 26, 2012 (received for review February 27, 2012)

Generation and motion of dislocations and twinning are the main mechanisms of plastic deformation. A new mechanism of plastic deformation and stress relaxation at high strain rates (10^9 – 10^{12} s⁻¹) is proposed, under which virtual melting occurs at temperatures much below the melting temperature. Virtual melting is predicted using a developed, advanced thermodynamic approach and confirmed by large-scale molecular dynamics simulations of shockwave propagation and quasi-isentropic compression in both single and defective crystals. The work and energy of nonhydrostatic stresses at the shock front drastically increase the driving force for melting from the uniaxially compressed solid state, reducing the melting temperature by 80% or 4,000 K. After melting, the relaxation of nonhydrostatic stresses leads to an undercooled and unstable liquid, which recrystallizes in picosecond time scales to a hydrostatically loaded crystal. Characteristic parameters for virtual melting are determined from molecular dynamics simulations of Cu shocked/compressed along the $\langle 110 \rangle$ and $\langle 111 \rangle$ directions and Al shocked/compressed along the $\langle 110 \rangle$ direction.

high strain-rate plasticity | relaxation of non-hydrostatic stresses | thermodynamics under uniaxial straining

Generation and motion of dislocations, twinning, and crystal–crystal phase transformations are the main mechanisms of plastic deformation and relaxation of nonhydrostatic stresses that are reflected in the deformation–mechanism maps (1, 2). Recent large-scale nonequilibrium molecular dynamics (NEMD) simulations of shockwave propagation in fcc metallic single crystals have revealed that for wave propagation along the $\langle 110 \rangle$ and $\langle 111 \rangle$ directions, melting occurs at temperatures below the equilibrium melt temperature $T_m(p)$ at the corresponding shock pressure p —e.g., for Cu by 20% in ref. 3 and by 7–8% ($\pm 4\%$) in ref. 4. However, for shockwaves along the $\langle 001 \rangle$ direction, superheating is observed. A possible mechanism for the observed melting below $T_m(p)$ has been attributed to solid-state disordering due to high defect densities. Indeed, a small reduction in the melt temperature due to defects has been reported (5). It has also been argued that anomalous plastic flow rather than bulk melt can explain the experimentally observed low melt temperatures of Ta under pressure (6). Here, we propose a new deformation mechanism, under which melting can occur at temperatures much below $T_m(p)$ in materials subjected to high deviatoric stresses (such as those produced under shock loading and isentropic deformation) and compete with defect nucleation mechanisms, as will be shown here in the case of metals. We have developed a thermomechanical theory of melting under uniaxial deformation that predicts extremely large driving forces. The thermodynamic driving force for melting is due to the energy and work of nonhydrostatic stresses. The theory is quite general and not material-specific, and it is most applicable at deformation rates sufficiently high, where melting may proceed at rates faster than traditional mechanisms of plasticity. As a proof of concept, we have systematically studied melting under high strain rates in two fcc metals, Cu and Al, employing molecular dynamics (MD) methods that simulate quasi-isentropic and shockwave loading conditions.

These simulations confirm for the first time that melting can occur at temperatures much below (by 80% or 4,000 K) $T_m(p)$. After melting, the nonhydrostatic stresses relax, leading to an undercooled and unstable liquid, which for the metals studied here recrystallizes in ps time scales. Because the conditions for melting (nonhydrostatic stresses) disappear upon melting, and because of the short time scale involved, we have termed this new deformation mechanism virtual melting (VM). Because fcc metals can be easily deformed by traditional dislocation and twinning mechanisms, the strain rates at which VM is observed and confirmed via our MD simulations of Cu and Al crystals are necessarily high (approximately 10^9 – 10^{12} s⁻¹) and represent an upper bound in the regime of strain rates to study and confirm our thermodynamic predictions. For materials with suppressed plasticity (such as Si, Ge, high-strength materials, alloys, or complex organic molecules), VM may very well be observed at much lower strain rates. Because the thermodynamic VM formalism is quite general, in what follows we will primarily discuss our results for Cu and Al shocked or quasi-isentropically compressed along the $\langle 110 \rangle$ direction and Cu shocked or quasi-isentropically compressed along the $\langle 111 \rangle$ direction. Simulation details are provided in *SI Appendix*. We find that the reduction of the melt temperature correlates with the magnitude of the nonhydrostatic (shear) stress at the shock front, which is consistent with thermodynamics.

Results and Discussion

Development of Thermodynamics of Melting Under Nonhydrostatic Conditions (see details in *SI Appendix*). Fig. 1*A* shows, by way of example, the stress σ_1 –uniaxial strain curve for a Cu single crystal loaded in the $\langle 110 \rangle$ direction. The data was obtained from quasi-isentropic MD simulations employing a well-tested embedded atom method (EAM) potential for Cu (7). Because in a planar shock, the two lateral strains are zero, the uniaxial strain $\varepsilon = l/l_0 - 1$ is equal to the volumetric strain, where l_0 and l are the initial and the current lengths of the sample, respectively. Melting starts at strain $\varepsilon = \varepsilon^*$ and stress $\sigma_1 = \sigma_1^m$, and it ends at strain $\varepsilon = \varepsilon^m$ and at the same stress σ_1 . Because the transformation proceeds under a variable stress tensor, classical thermodynamic approaches based on thermodynamic potential differences and thermodynamic equilibrium across an interface (8–10) are not applicable. In fact, the reduction of the thermodynamic melt temperature of the stress-free solid, $T_m(0)$, caused by deviatoric stresses was estimated to be just 1 K (8, 10), which is why it was not considered as a possible reason for the reduction in $T_m(0)$ in shockwaves. We here will consider a homogeneous transformation process in a finite volume, expanding on our advanced thermodynamic approach to crystal–crystal transformations (11, 12). Because melting is assumed to be the only

Author contributions: V.I.L. and R.R. performed research and wrote the paper.

The authors declare no conflict of interest.

*This Direct Submission article had a prearranged editor.

¹To whom correspondence should be addressed. E-mail: vlevitas@iastate.edu.

This article contains supporting information online at www.pnas.org/lookup/suppl/doi:10.1073/pnas.1203285109/-DCSupplemental.

Solid-state disordering has been proposed as the main mechanism of pre-melting in shock along the $\langle 110 \rangle$ and $\langle 111 \rangle$ orientations in Cu single crystals (4). In order to distinguish between a hot, amorphous solid or a supercooled liquid, the self-diffusion coefficient of the liquid region behind the shock front was computed from the mean-squared displacement. Fig. 4C shows the diffusion coefficient as a function of temperature at a pressure of 145 GPa for the liquid state of the EAM model Cu used in this work. Also shown is the diffusion coefficient of a region behind the shock front in a Cu slab shocked along the $\langle 111 \rangle$ direction to the same pressure. Because all points belong to the same Arrhenius line, these results confirmed that the region behind the shock front is a supercooled liquid rather than an amorphous solid. Note that VM was observed for isothermal $\langle 111 \rangle$ loading of Cu even at 300 K (Table S1 in SI Appendix)—i.e., at $T \approx 0.055 T_m(p)$. However, recrystallization is so fast that the diffusion coefficient could not be determined.

Conclusions

At high strain rates ($\dot{\epsilon} \sim 10^9 - 10^{12} \text{ s}^{-1}$ in metals) and high shear stresses, VM can compete with traditional defect nucleation mechanisms and therefore should be incorporated in the deformation-mechanism maps (1, 2). This prediction is based on a new thermomechanical theory of melting under uniaxial straining that is quite general and that can be applied to any material subjected to strain rates sufficiently large in order to allow melting to proceed faster than traditional mechanisms of plasticity. Virtual melting has been confirmed for the first time by MD simulations for the most critical case of fcc metals. For materials with suppressed plasticity, VM may be observed at lower strain rates and stresses than the ones sampled here [e.g., in a recent MD study (16) deformation of organic α -HMX crystal is shown to occur through generation and motion of dislocations for shock strengths up to 14 GPa and via formation of amorphous shear nanobands at higher pressure, which may be related to VM]. Our thermodynamic approach can be extended for amorphization and

sublimation as well as for arbitrary 3D loading, in particular for pressure and shear experiments. The concept of the VM was introduced in refs. (17–20) as an intermediate step in crystal–crystal, crystal–amorphous, and crystal–gas transformations. Here, however, VM was for the first time directly observed in MD simulations of plastic straining. The driving force for VM in phase transformations in refs. (17–20) is due to the relaxation of the deviatoric stresses and also disappears upon melting, as in the case of VM here. This suggests that our results here indirectly support the plausibility of VM in phase transformation as well. Finally, while the sampled compression rates in our simulations of Cu and Al were necessarily high, they are close to what can be achieved in laser-driven shock experiments (21). However, due to the short time scales additional efforts are required for experimental verification of VM, particularly in metals. Such regimes are also relevant for nuclear explosion and meteorite impact as well as for planned experiments in large laser facilities such as the National Ignition Facilities at the Lawrence Livermore National Laboratory in the United States and the Laboratoire pour l'Utilisation des Lasers Intenses in France.

Materials and Methods

We have performed multimillion atom NEMD simulations of shockwave compression as well as smaller, Hugoniot-method (22) and MD simulations of quasi-isentropic compression (15). The NEMD simulations comprised up to 12 million atoms arranged in a rectangular slab with periodic boundary conditions in the transverse directions. The procedure used to initiate a shockwave of a given strength is detailed in ref. 23. The systems studied were Cu and Al single crystals as well as Cu crystals with pre-existing defects. A detailed description of the MD simulations and methods is available in SI Appendix.

ACKNOWLEDGMENTS. V.I.L. acknowledges support from the National Science Foundation and Army Research Office. R.R. would like to thank T.C. Gemann, B. L. Holian and J. E. Hammerberg (Los Alamos National Laboratory) for valuable ideas and helpful discussions. Part of this work has been supported by the US Department of Energy under contract DE-AC52-06NA25396.

1. Frost HJ, Ashby MF (1989) *Deformation-Mechanism Maps* (Pergamon Press, New York).
2. Meyers MA, Vohringer O, Lubarda VA (2001) The onset of twinning in metals: A constitutive description. *Acta Mater* 49:4025–4039.
3. Ravelo R, Germann TC, Holian BL, Lomdahl PS (2006) Directional-dependence in shock-induced melting of FCC metals. *AIP Conf Proc* 845:270–273.
4. An Q, et al. (2008) Melting of Cu under hydrostatic and shock wave loading to high pressures. *J Phys Cond Mat* 20:095220.
5. Alsayed AM, et al. (2005) Premelting at defects within bulk colloidal crystals. *Science* 309:1207–1210.
6. Wu CJ, Soderlind P, Glosli JN, Klepeis JE (2009) Shear-induced anisotropic plastic flow from body-centered-cubic tantalum before melting. *Nat Mater* 8:223–228.
7. Mishin Y, et al. (2001) Structural stability and lattice defects in copper: Ab initio, tight-binding, and embedded-atom calculations. *Phys Rev B Condens Matter Mater Phys* 63:224106.
8. Grinfeld MA (1991) *Thermodynamic Methods in the Theory of Heterogeneous Systems* (Longman, Sussex, UK).
9. Grinfeld MA (1980) On the thermodynamic stability of material. *Dokl Akad Nauk SSSR* 251:824–828.
10. Sekerka RF, Cahn JW (2004) Solid-liquid equilibrium for non-hydrostatic stress. *Acta Mater* 52:1663–1668.
11. Levitas VI (2000) Structural changes without stable intermediate state in inelastic material. Parts I and II. *Int J Plasticity* 16:805–892.
12. Levitas VI (1998) Thermomechanical theory of martensitic phase transformations in inelastic materials. *Int J Solids Struct* 35:889–940.
13. Ten Wolde PR, Ruiz-Montero MJ, Frankel D (1995) Numerical evidence for bcc ordering at the surface of a critical fcc nucleus. *Phys Rev Lett* 75:2714–2717.
14. Steinhardt PJ, Nelson DR, Ronchetti M (1983) Bond-orientational order in liquids and glasses. *Phys Rev B Condens Matter Mater Phys* 28:784–805.
15. Ravelo R, Holian BL, Germann TC (2009) High strain rates effects in quasi-isentropic compression of solids. *AIP Conf Proc* 1195:825–830.
16. Jaramillo E, Sewell TD, Strachan A (2007) Atomic-level view of inelastic deformation in a shock loaded molecular crystal. *Phys Rev B Condens Matter Mater Phys* 76:064112.
17. Levitas VI, Henson BF, Smilowitz LB, Asay BW (2004) Solid-solid phase transformation via virtual melting significantly below the melting temperature. *Phys Rev Lett* 92:235702.
18. Levitas VI, Henson BF, Smilowitz LB, Asay BW (2006) Solid-solid phase transformation via internal stress-induced virtual melting, significantly below the melting temperature. Application to HMX energetic crystal. *J Phys Chem B* 110:10105–10119.
19. Levitas VI (2005) Crystal-amorphous and crystal-crystal phase transformations via virtual melting. *Phys Rev Lett* 95:075701.
20. Levitas VI, Altukhova N (2009) Sublimation via virtual melting inside an elastoplastic material. *Phys Rev B Condens Matter Mater Phys* 79:212101.
21. Crowhurst JC, Armstrong MR, Knight KB, Zaug JM, Behymer EM (2011) Invariance of the dissipative action at ultrahigh strain rates above the strong shock threshold. *Phys Rev Lett* 107:144302.
22. Ravelo R, Holian BL, Germann TC, Lomdahl PS (2004) Constant-stress Hugoniot method for following the dynamical evolution of shocked matter. *Phys Rev B Condens Matter Mater Phys* 70:014103.
23. Holian BL, Lomdahl PS (1998) Plasticity induced by shock waves in nonequilibrium molecular-dynamics simulations. *Science* 80:2085–2088.

Supporting Information

Virtual Melting: A New Mechanism of Stress Relaxation Under High Strain Rate Loading

Valery I. Levitas^a and Ramon Ravelo^b

^a*Iowa State University, Departments of Aerospace Engineering, Mechanical Engineering, and Material Science and Engineering, Ames, Iowa 50011, USA;*

^b*Physics Department and Materials Research Institute, University of Texas, El Paso, TX 79968 and Computational Physics Division, Los Alamos National Laboratory, Los Alamos, NM 87545*

1. Methods of Advanced Thermodynamic Calculations

Since melting is considered the only dissipative process, the thermodynamic driving force per unit unloaded volume for the melting for isothermal loading is equal to the total dissipation [1, 2]:

$$X_m = W + \Delta s(T - T_m(0)) + (\psi_c^h(\varepsilon^*) - \psi_m^h(\varepsilon^m)) + \psi_c^{dev}(\varepsilon^*). \quad (1)$$

Here, $W = \int_{\varepsilon^*}^{\varepsilon^m} \sigma_1(\varepsilon) d\varepsilon$ is the the transformation work, which takes into account the actual stress-strain curve $\sigma_1(\varepsilon)$ during the melting; ψ^h and ψ^{dev} are the elastic energy of hydrostatic and deviatoric stresses (strains); Δs is the jump in entropy; T is the temperature at which the melting is started (at $\varepsilon = \varepsilon^*$); $T_m(0)$ is the thermodynamic melting temperature for stress-free solid; and subscripts c and m are for crystalline and molten states, respectively.

Let $p_c(\varepsilon)$ and $p_m(\varepsilon)$ be the equations of state of the crystalline and molten phases (Fig. 1). The equation of state for melt starts at point ($\varepsilon = \varepsilon_0$ and $\sigma_1 = 0$), where $\varepsilon_0 < 0$ is the volumetric transformation strain at melting at pressure $p = 0$. Then,

$$\psi_c^h(\varepsilon^*) = \int_0^{\varepsilon^*} p_c d\varepsilon; \quad \psi_c^{dev}(\varepsilon^*) + \psi_c^h(\varepsilon^*) = \int_0^{\varepsilon^*} \sigma_1 d\varepsilon; \quad \psi_m^h(\varepsilon^m) = \int_{\varepsilon_0}^{\varepsilon^m} p_m d\varepsilon, \quad (2)$$

and

$$X_m = \int_0^{\varepsilon^m} \sigma_1 d\varepsilon - \int_{\varepsilon_0}^{\varepsilon^m} p_m d\varepsilon + \Delta s(T - T_m(0)). \quad (3)$$

Geometrically, the mechanical driving force for melting is equal to the difference between the areas under the stress-strain curve for $\sigma_1(\varepsilon)$ $\{Oabc\varepsilon^m\}$ and for $p_m(\varepsilon)$ $\{\varepsilon_0c\varepsilon^m\}$ (Fig. 1). For melting under constant temperature and hydrostatic pressure $p = \sigma_1$, the condition for thermodynamic equilibrium is

$$X^h = \sigma_1(\varepsilon_m - \bar{\varepsilon}) + \Delta s(T_m(\sigma_1) - T_m(0)) + (\psi_c^h(\bar{\varepsilon}) - \psi_m^h(\varepsilon_m)) = 0, \quad (4)$$

where $T_m(\sigma_1)$ is the equilibrium melting temperature under hydrostatic pressure $p = \sigma_1$, $\bar{\varepsilon} = \varepsilon_c(\sigma_1)$, $\varepsilon_c(p)$ and $\varepsilon_m(p)$ are the inverse equations of state for crystal and melt. The magnitude of the negative mechanical part of X_h is $\{O\varepsilon_0cd\}$ (Fig. 1). It follows from Eq. (4):

$$T_m(\sigma_1) = T_m(0) + (\sigma_1(\bar{\varepsilon} - \varepsilon_m) - (\psi_c^h(\bar{\varepsilon}) - \psi_m^h(\varepsilon_m))) / \Delta s. \quad (5)$$

Expressing $\Delta s T_m(0)$ from Eq. (4) and substituting it in Eq. (1), we obtain

$$X_m = W + \sigma_1(\bar{\varepsilon} - \varepsilon_m) + \Delta s(T - T_m(\sigma_1)) + (\psi_c^h(\varepsilon^*) - \psi_c^h(\bar{\varepsilon})) + \psi_c^{dev}(\varepsilon^*). \quad (6)$$

Then, the condition $X_m = 0$ results in

$$\begin{aligned} T_m^{nh} &= T_m(\sigma_1) - (\psi_c^{dev}(\varepsilon^*) + W + \sigma_1(\bar{\varepsilon} - \varepsilon^m) - (\psi_c^h(\bar{\varepsilon}) - \psi_c^h(\varepsilon^*))) / \Delta s = \\ T_m(\sigma_1) &- \left(\int_0^{\varepsilon^m} \sigma_1 d\varepsilon - \int_0^{\bar{\varepsilon}} p_c d\varepsilon + \sigma_1(\bar{\varepsilon} - \varepsilon^m) \right) / \Delta s. \end{aligned} \quad (7)$$

Geometrically, additional driving force for melting due to nonhydrostatic loading (the term in parentheses in Eq. (7)) is equal to the difference between the areas under the stress-strain curve $\sigma_1(\varepsilon)$ $\{Oabcd\}$ and the equation of state $p_c(\varepsilon)$ for crystal $\{Od\}$. All parameters for melting of Cu and Al for loading in the $\langle 110 \rangle$ direction and for Cu loading in the $\langle 111 \rangle$ direction are given in Table 1S.

Table 1S. Parameters for crystal loading (ε^* , ε^m , $\bar{\varepsilon}$, and σ_1^m , see Figs. 1 and 4S), maximum strain rate $\dot{\varepsilon}_{\max}$, initial T^* and final T_f temperatures, as well as melting temperature under hydrostatic conditions $T_m(\sigma_1^m)$ and decrease in melting temperature due to nonhydrostatic loading ΔT_m .

	ε^*	ε^m	$\bar{\varepsilon}$	$\dot{\varepsilon}_{\max}$	σ_1^m	T^*	T_f	$T_m(\sigma_1^m)$	ΔT_m
				ps^{-1}	GPa	K	K	K	K
Cu <110>	0.214	0.324	0.351	2.48	179.1	325	3084	5087	10074
Cu <111>	0.297	0.360	0.369	4.3	204.9	300	300	5434	9197
Cu <111>	0.301	0.353	0.375	3.97	215.1	197	2604	5565	8022
Al <110>	0.227	0.356	0.386	3.87	98.17	305	2711	3544	9945

Table 2S. Parameters in Murnaghan's (8) and Simon's (11) equations in Supplementary Materials.

	p_0	b	T_0	α	β
	GPa		K	GPa	
Cu	39.096	3.98	1327	15.3691	0.529458
Al	33.576	2.81	324	2.56529	0.647822

Table 3S. Parameters in Eq.(14) in Supplementary Materials for the reduction in melting temperature due to nonhydrostatic loading.

	T_f	A_σ	B_σ	C_σ	A_ε	B_ε	C_ε
	K	K	K/GPa	K/GPa ²	K	K	K
Cu <110>	3084	-1128	44.67	0.1008	4174	-82665	517956
Cu <111>	300	-1845	64.52	0.0518	-2182	20997	59602
Cu <111>	2604	-1137	42.24	0.0020	-299	-2684	101753
Al <110>	2711	-441	15.26	0.9295	5162	-96069	493689

The Murnaghan's equation of state for crystal, $p_c(\varepsilon)$, its inverse form, and the corresponding expressions for ψ_c^h and ψ_c^{dev} are:

$$p_c = p_0((1 - \varepsilon)^{-b} - 1); \quad \varepsilon = 1 - \left(1 + \frac{p_c}{p_0}\right)^{-1/b}, \quad (8)$$

$$\psi_c^h = \int_0^\varepsilon p d\varepsilon = \frac{p_0}{b-1} ((1 - \varepsilon)^{b-1} - \varepsilon(b-1) - 1), \quad \psi_c^{dev} = \int_0^{\varepsilon^*} \sigma_1 d\varepsilon - \psi_c^h(\varepsilon^*), \quad (9)$$

where parameters p_0 and b for Cu and Al are given in Table 2S.

The jump in entropy Δs versus pressure p along the melting line $T_m(p)$ is found using the Clausius-Clapeyron relation

$$\Delta s = -\varepsilon_v / (dT_m(p)/dp), \quad (10)$$

where ε_v is the volumetric strain during the melting under the pressure (equal to ε_0 for $p = 0$). Since we consider cubic crystals with isotropic thermal expansion, the effect of deviatoric stresses on entropy will be neglected. The melting temperature versus pressure is found according to the Simon equation:

$$T_m = T_0(1 + p/\alpha)^\beta, \quad (11)$$

with parameters T_0 , α , and β given in Table 2S for Cu and Al. The volume change during the melting $\varepsilon_v < 0$ along the melting line was calculated using MD simulations at constant temperature and pressure and approximated by the functions

$$|\varepsilon_v| = 0.008915 + 0.95820/p - 4.4612/p^2 \quad (12)$$

for Al and

$$|\varepsilon_v| = 0.013712 + 1.14436/p - 19.3125/p^2 + 105.80245/p^3 \quad (13)$$

for Cu. Substitution of Eqs. (11), (12), or (13) in Eq. (10) gives us jump in entropy. Functions $|\varepsilon_v|$ and Δs vs. pressure are shown in Figs. 1S and 2S for Cu and Al, respectively. While the

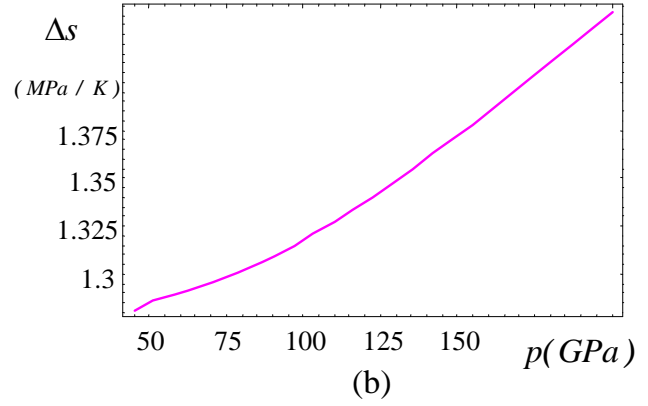
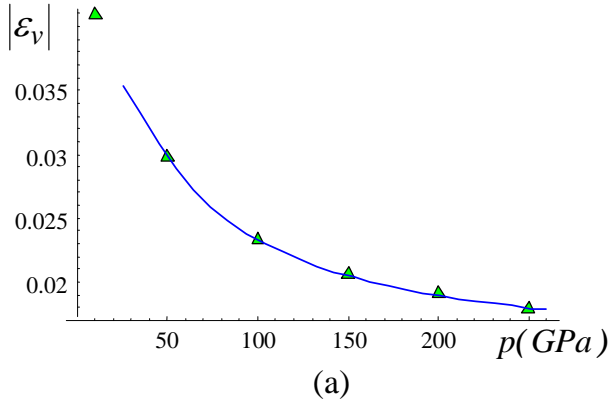


Figure 1S. (a) Jump in volumetric strain vs. pressure calculated using MD constant pressure and temperature simulations for Cu. (b) Jump in entropy during melting vs. pressure calculated using Clausius-Clapeyron equation (10) for Cu.

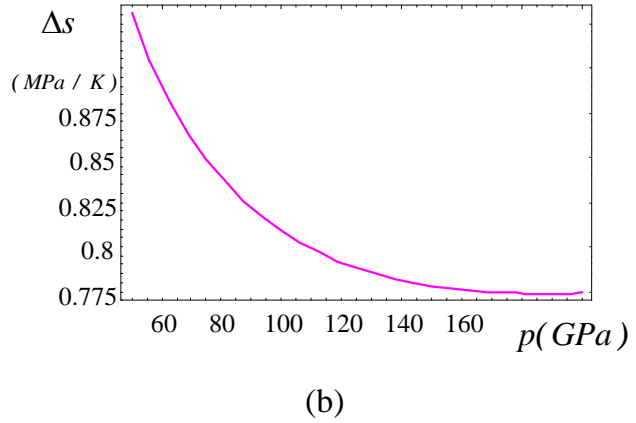
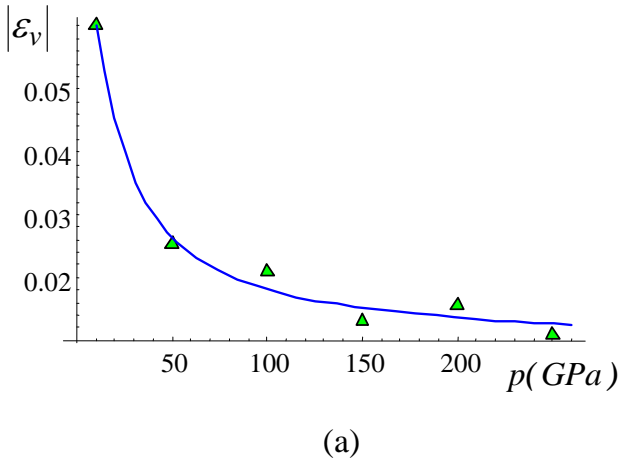


Figure 2S. (a) Jump in volumetric strain vs. pressure calculated using MD constant pressure and temperature simulations for Al. (b) Jump in entropy during melting vs. pressure calculated using Clausius-Clapeyron equation (10) for Al.

pressure dependence of Δs is very weak, it is interesting to note that it has different slopes for Cu and Al.

To calculate the melting temperature decrease for lower strains ε^* and corresponding stress $\sigma_1(\varepsilon^*)$, one needs to know the stress-strain curve $\sigma_1(\varepsilon)$ for elastic uniaxial loading (we will take it from Fig. 1, but it can be found phenomenologically if pressure dependence of elastic constants is known), the equation of state for solid $p(\varepsilon_c)$, and the stress strain curve $\sigma_1(\varepsilon)$ during melting, which has to be determined by MD simulation for each ε^* separately. To avoid additional MD simulations, we take into account that the reduction in σ_1 during the melting (line *abc* in Fig. 1) results in multiplication of work under constant stress $\sigma_1(\bar{\varepsilon} - \varepsilon^*)$ by a factor $h = 0.8831$ for Al (or $h = 0.8847$ for Cu) for $\langle 110 \rangle$ loading, which we used for all smaller ε^* . For $\langle 111 \rangle$ loading of Cu, we obtain $h = 0.9504$ for $T_f = 300K$ and $h = 0.8311$ for $T_f = 2604K$. The calculated melting temperature decrease (Eq. (7)) for lower strains ε^* and corresponding stress $\sigma_1(\varepsilon^*)$ can be approximated in the form

$$\Delta T_m = T_m(\sigma_1) - T_m^{nh}(\sigma_1) = A_\sigma + B_\sigma \sigma_1 + C_\sigma \sigma_1^2 = A_\varepsilon + B_\varepsilon \varepsilon^* + C_\varepsilon \varepsilon^{*2}, \quad (14)$$

where all constants are listed in Table 3S.

2. Methods of Molecular Dynamics Simulations

We performed multi-million atom non-equilibrium molecular dynamics (NEMD) simulations of shock wave compression, as well as smaller, Hugoniotat, and molecular dynamics (MD) simulations of quasi-isentropic compression to explore the dynamical evolution of the shocked state as a function of shock compression and crystallographic direction. The NEMD simulations comprised up to 12 million atoms arranged in a rectangular slab with periodic boundary conditions in the transverse directions. We employed the high-performance parallel molecular dynamics code

SPaSM [3] for the multi-million NEMD simulations. The procedure used to initiate a shock wave of a given strength is detailed in Ref. [4]: the crystal impacts an infinitely massive piston with a velocity $-u_p$, which produces a shock wave that propagates away from the piston with velocity $u_s - u_p$, u_s being the shock velocity. The NEMD sampled time scales were nominally of the order of 20-40 ps.

These simulations were augmented by constant-stress Hugoniotat simulations comprising 10^5 atoms arranged approximately in a cube. Details of the method can be found in Ref. [5]. We also carried out quasi-isentropic compression simulations, in which the system was uniaxially and homogeneously compressed to a final uniaxial strain using a specified time-profile for the strain-rate. Details of this method are given in [6].

The systems we chose to study were copper and aluminum single crystals shocked or quasi-isentropically compressed along the $\langle 110 \rangle$ direction and aluminum single crystal along the $\langle 111 \rangle$ direction. These crystallographic directions are known to produce large shear stresses with strain. The atomic interactions in the Cu and Al simulations were described using the well-tested embedded-atom method (EAM) models for Cu [7] and Al [8].

3. Results of additional MD simulations

1. The role of high shear stresses on the lowering of the melt temperature can be studied in greater detail via quasi-isentropic compression simulations, where the final compressive strain can be fixed, while the uniaxial strain-rate is varied. Using these types of simulations, we carried out a systematic study of virtual melting in both single and defective Cu crystals. We employed approximately cubic samples with 1.2×10^5 to 1.5×10^6 atoms and periodic boundary conditions. The final strain was fixed, and the strain rate was varied over 3 decades (from 2.5×10^9 to $2.5 \times 10^{12} \text{ s}^{-1}$). As shown in Fig. 4 for Cu, along $\langle 110 \rangle$, the shear stress increases rapidly with

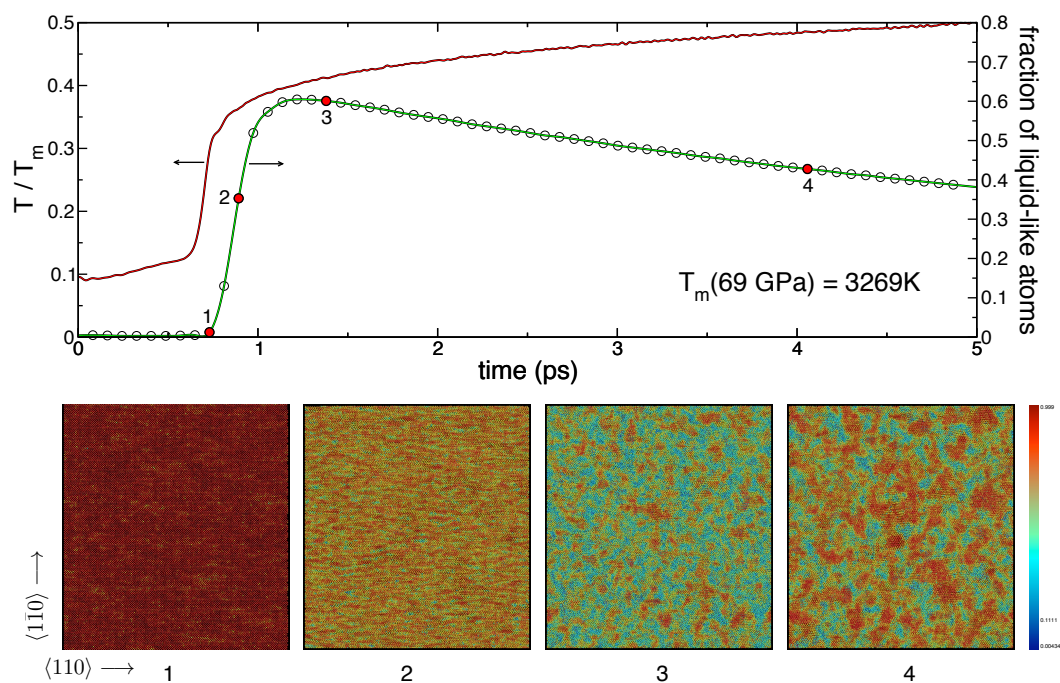


Figure 3S. 1.35-million-atom simulation of Cu quasi-isentropically compressed along $\langle 110 \rangle$ at an average strain rate of $2.5 \times 10^{11} \text{ s}^{-1}$ to a final strain of 0.20. The temperature profile (upper line) has been normalized by the equilibrium melt temperature at the final pressure (69 GPa). The fraction of liquid-like atoms (lower line) was computed from the order parameter q_6 . The atomic profiles numbered at the bottom corresponds to the times numbered along the path. Atoms are colored according to q_6 : solid (red) and liquid (blue).

compression. Under quasi-isentropic compression and at sufficiently high strain rates, we find that the system can melt at $T \simeq 0.35T_m(p)$ (Fig. 3S). Figure 3S also shows a sequence of snapshots of the atomic configurations in a 1.35-million-atom single crystal Cu simulation in which the system was quasi-isentropically compressed along the $\langle 110 \rangle$ orientation at an average strain rate of $2.5 \times 10^{11} \text{ s}^{-1}$ to a final strain of 0.20. Also shown is the temperature (red line) normalized by the equilibrium melt temperature at the equilibrium pressure (69 GPa). The fraction of liquid atoms (green line) as a function of time was computed by following the evolution of the local order parameter q_6 and evaluating the fraction of atoms with a value less than 0.6. It takes about 0.8 ps to compress the sample to strain of 0.20 at $\dot{\epsilon} = 0.25 \text{ ps}^{-1}$. At the point labeled 1 in Fig. 3S, the atoms are still in an elastic and uniaxially compressed state, with a very high elastic energy corresponding to the highest shear stress (45 GPa) along the path. From point 1 to point 3, the system transforms from uniaxially compressed elastic solid to an isotropic state due to virtual melting. The virtual melting is partial at this strain and strain rate, and the liquid regions (blue atoms) coarsened rapidly. At the point labeled 3, the material is more isotropic, the elastic energy has been reduced significantly, and the temperature has increased due to the enthalpy difference between the isotropic liquid and the uniaxially compressed elastic solid. The time scale for this conversion is less than 1 ps. The decrease of the fraction of liquid atoms with time is caused by re-solidification from the melt (red atoms, point 4 along the path) followed by further reduction in the shear stress and an increase in temperature. From the enthalpy differences between the uniaxially compressed solid, supercooled liquid, and isotropic solid, the temperature profile as a function of time can be evaluated with excellent agreement with the simulations.

2. In addition, crystallization kinetics unambiguously suggests that the disordering represents the virtual melt rather than amorphization. Increase in temperature increases thermal fluctuations and promotes kinetics of crystallization from both melt and glass. However, the driving

force for crystallization of the melt and glass is the increasing function of $T_m - T$ and $T - T_g > 0$, respectively (where T_g is the glass transition temperature); thus temperature has opposite effect on these driving forces. We assume that T_g is below temperature at the end of our calculations, otherwise, there is no sense to talk about the crystallization of glass. For glass, the driving force for crystallization increases with temperature growth and crystallization rate has to be faster with increasing temperature. For melt, the driving force reduces with temperature increase and (if thermodynamic effect exceeds the kinetic one) crystallization rate may decrease with growing temperature. Since in all our MD simulations the crystallization rate decreased with the growing temperature, we can conclude that the disordered state is the virtual melt rather than glass.

3. For strain rate smaller than some threshold, melting occurs heterogeneously rather than in the entire volume (Fig. 3S). The volume fraction of disordered regions decreases with the decrease in strain rate. Note that if the remaining crystals are surrounded by melt and are under hydrostatic conditions, the total energy will be smaller than for complete melting, and the driving force will be even larger. This is because the energy of hydrostatically loaded crystal is much smaller than the energy of the melt below melting temperature. Crystallization time drastically depends on the existence of residual crystalline clusters, which can serve as nucleation sites. The higher are the shock strength (or strain rate) and temperature, the less probability there is of finding residual crystalline clusters in melt. Much more time is required for homogeneous nucleation of the crystal phase.

4. Fig. 4S shows the stresses and temperature evolution, and prescribed strain rate vs. uniaxial strain obtained using MD simulations for $\langle 110 \rangle$ shock loading of Al, similar to Fig. 1 for Cu. A well-tested EAM potential for Cu [8] was used.

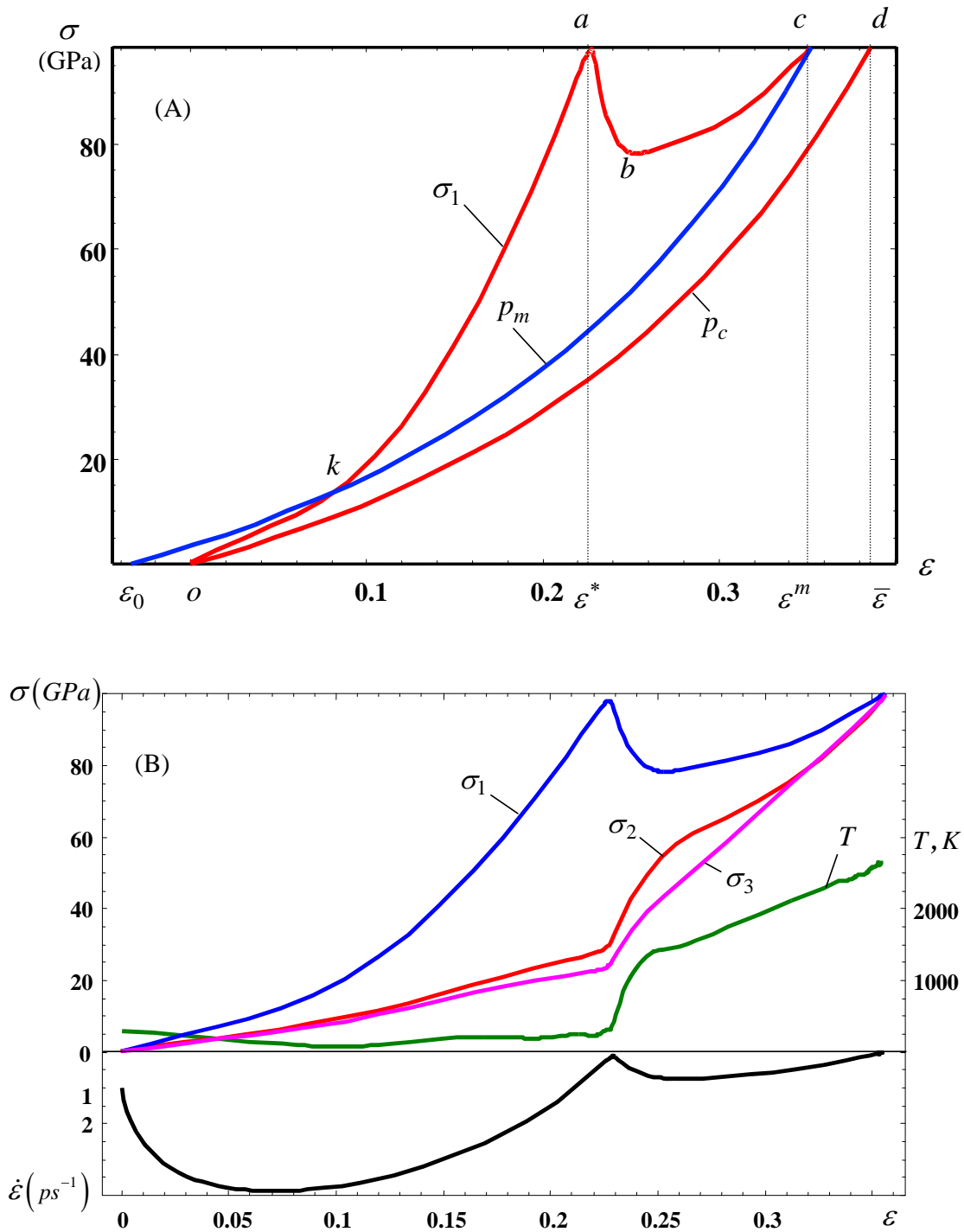


Figure 4S. (A) Stress-uniaxial strain curve of an Al crystal until melting (σ_1 , the same as in Fig. 4S, B) and equations of state of molten (p_m) and crystalline (p_c) phases. Area between curves $\{Oabcd\}$ and $\{Od\}$ is the additional driving force for melting due to nonhydrostatic loading. (B) Variation of normal stresses σ_i , temperature, and prescribed strain rate vs. uniaxial strain obtained using MD simulations for $\langle 110 \rangle$ shock loading of Al.

5. Supporting movie

Cu single crystal compressed quasi-isentropically along the $\langle 111 \rangle$ direction (out of plane) at a strain rate of $3 \times 10^{11} s^{-1}$ to a final uniaxial strain of 33% ($\sigma_1=174$ GPa) is shown. Axis x is along the $\langle 1\bar{1}0 \rangle$ direction and axis y is along the $\langle 11\bar{2} \rangle$ direction. The cross section of atomic configuration in the left panel is $10 \text{ nm} \times 10 \text{ nm}$. Only atoms within a 1.7 nm thick slice are shown for clarity. Atoms are colored according to q_6 [9, 10] (red atoms are solid, green atoms are liquid). The right panel shows the time evolution of the temperature (normalized by the equilibrium melt temperature at the corresponding pressure), pressure (p) and shear stress (τ).

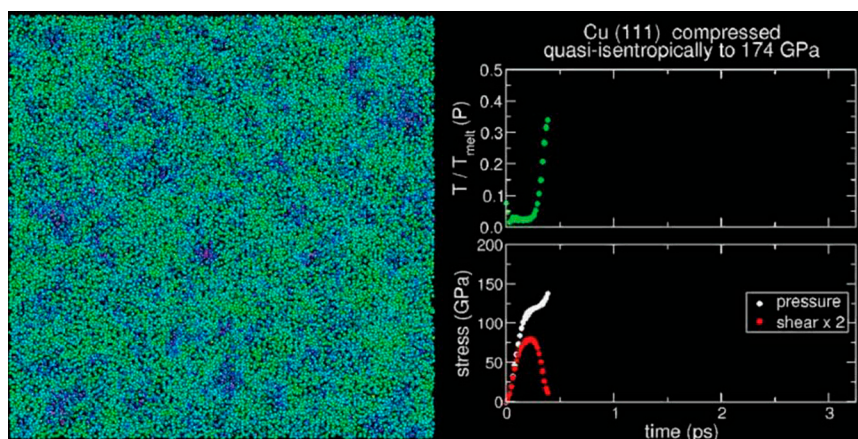
References

- [1] Levitas VI (1998) Thermomechanical Theory of Martensitic Phase Transformations in Inelastic Materials. *Int. J. Solids and Structures* 35: 889-940.
- [2] Levitas VI (2000) Structural Changes Without Stable Intermediate State in Inelastic Material. Parts I and II. *Int. J. Plasticity* 16: 805-849 and 851-892.
- [3] Lomdahl PS, Tamayo P, Grnbech-Jensen N and Beazley DM (1993), *Proceedings of Supercomputing 93*, G. S. Ansell, Ed. (IEEE Computer Society Press, Los Alamitos, CA), 520527.
- [4] Holian BL and Lomdahl PS (1998) Plasticity induced by shock waves in nonequilibrium molecular-dynamics simulations. *Science* 80: 2085-2088.
- [5] Ravelo R, Holian BL, Germann TC, Lomdahl PS (2004) Constant-Stress Hugoniot Method for Following the Dynamical Evolution of Shocked Matter. *Phys. Rev B* 70: 014103.
- [6] Ravelo R, Holian BL and Germann TC (2009) High Strain Rates Effects in Quasi-Isentropic Compression of Solids. *AIP Conf. Proc.* 1195: 825-830.

- [7] Mishin Y et al. (2001) Structural Stability and Lattice Defects in Copper: Ab Initio, Tight-Binding, and Embedded-Atom Calculations. *Phys. Rev. B* 63: 224106.
- [8] Angelo JE, Moody NR and Baskes MI (1995) Trapping of Hydrogen to Lattice-Defects in Nickel. *Model. Simul. Mater. Sci. Eng.* 3: 289-307.
- [9] Ten Wolde PR, Ruiz-Montero MJ, and Frankel D (1995) Numerical Evidence for bcc Ordering at the Surface of a Critical fcc Nucleus. *Phys. Rev. Lett.* 75: 2714-2717.
- [10] Steinhardt PJ, Nelson DR, and Ronchetti M (1983) Bond-Orientational Order in Liquids and Glasses. *Phys. Rev. B* 28: 784-805.

Supporting Information

Levitas and Ravelo 10.1073/pnas.1203285109



Movie S1. Cu single crystal compressed quasi-isotropically along the $\langle 111 \rangle$ direction (out of plane) at a strain rate of $3 \times 10^{11} \text{ s}^{-1}$ to a final uniaxial strain of 33% ($\sigma_1 = 174 \text{ GPa}$) is shown. Axis x is along the $\langle 110 \rangle$ direction and axis y is along the $\langle 112 \rangle$ direction. The cross section of atomic configuration in the left panel is $10 \text{ nm} \times 10 \text{ nm}$. Only atoms within a 1.7 nm thick slice are shown for clarity. Atoms are colored according to q_6 (1, 2) (red atoms are solid, green atoms are liquid). The right panel shows the time evolution of the temperature (normalized by the equilibrium melt temperature at the corresponding pressure), pressure (p) and shear stress (τ).

1 Ten Wolde PR, Ruiz-Montero MJ, Frankel D (1995) Numerical evidence for bcc ordering at the surface of a critical fcc nucleus. *Phys Rev Lett* 75:2714–2717.

2 Steinhardt PJ, Nelson DR, Ronchetti M (1983) Bond-orientational order in liquids and glasses. *Phys Rev B Condens Matter Mater Phys* 28:784–805.

[Movie S1 \(MOV\)](#)